Band-gap engineering of rutile-structured SnO_2-GeO_2-SiO_2 alloy system

Hitoshi Takane [1,2,*] Yuichi Ota [3] Takeru Wakamatsu,[1] Tsutomu Araki,[4]
Katsuhisa Tanaka,[1] and Kentaro Kaneko [2,5,6,7,†]

[1]*Department of Material Chemistry, Kyoto University, Kyoto 615-8510, Japan*
[2]*Department of Electronic Science and Engineering, Kyoto University, Kyoto 615-8510, Japan*
[3]*Tokyo Metropolitan Industrial Technology Research Institute, Tokyo 135-0064, Japan*
[4]*Department of Electrical and Electronic Engineering, Ritsumeikan University, Shiga 525-8577, Japan*
[5]*Engineering Education Research Center, Kyoto University, Kyoto 615-8530, Japan*
[6]*Photonics and Electronics Science and Engineering Center, Kyoto University, Kyoto 615-8520, Japan*
[7]*Research Organization of Science and Technology, Ritsumeikan University, Shiga 525-8577, Japan*

(Received 12 May 2022; accepted 10 August 2022; published 26 August 2022)

Rutile-structured germanium oxide (r-GeO_2), an ultrawide band-gap (UWBG) semiconductor, is a promising candidate for future high-power electronics because of its excellent properties, including ambipolar dopability, high carrier mobilities, and a higher thermal conductivity than β-Ga_2O_3. In this paper, focusing on a wide variety of its applications, we propose an UWBG alloy system based on r-GeO_2 and other rutile-structured oxides (SnO_2-GeO_2-SiO_2) and clarify the electronic structure and electrical properties based on experiments and the first-principles calculations. Experimentally, (001)-oriented r-$Ge_xSn_{1-x}O_2$ alloy thin films with an entire range of Ge compositions (x) were grown by a mist chemical vapor deposition technique. Structural characterizations show that the fabricated r-$Ge_xSn_{1-x}O_2$ alloy films with $x \leqslant 0.96$ and the well-crystallized part of the film with $x = 1.00$ have uniform chemical compositions and the same epitaxial relations with r-TiO_2 (001) substrates. Transmission electron microscopy observations reveal that there are few dislocations in r-$Ge_{0.66}Sn_{0.34}O_2$ because of relatively small in-plane lattice mismatch. In contrast, many dislocations are observed near the film/substrate interface in r-$Ge_{0.96}Sn_{0.04}O_2$. Lattice constants of the alloys both along the a and c axes decrease with increase in Ge compositions. Their band gaps were determined by spectroscopic ellipsometry analysis, indicating that the band gaps increase as Ge compositions increase ($3.81 - 4.44$ eV) with a bowing parameter of 1.2 eV. The values of lattice constants and the trend of band-gap transitions obtained by calculations are in good agreement with those of experimentally obtained each other. Then we presented the calculated natural band alignments of r-$Ge_xSn_{1-x}O_2$ and r-$Ge_xSi_{1-x}O_2$ alloys, suggesting the possibility of p-type doping in r-GeO_2 and Ge-rich r-$Ge_xSn_{1-x}O_2$ and availability of r-SiO_2 and Si-rich r-$Ge_xSi_{1-x}O_2$ as a blocking layer of other rutile-structured devices. Finally, electrical measurements demonstrated n-type conductivities in r-$Ge_xSn_{1-x}O_2$ ($x \leqslant 0.57$).

DOI: 10.1103/PhysRevMaterials.6.084604

I. INTRODUCTION

Increasing demands for energy-saving societies have raised attention to ultrawide band-gap (UWBG) semiconductors, with a band gap (E_g) >3.4 eV as advanced materials for high-power and radiofrequency (RF) electronic devices as well as deep-ultraviolet optoelectronic devices [1]. For example, β-Ga_2O_3 ($E_g = 4.48-4.9$ eV) [2,3] is one of the most investigated UWBG materials due to the availability of its substrate as well as its large breakdown field. However, conventional UWBG materials including β-Ga_2O_3 have difficulties in effective ambipolar doping and conduction, which restricts full use of them for various applications.

Now there is great interest in rutile-structured germanium oxide (r-GeO_2), with $E_g = 4.44-4.68$ eV [4–6] comparable with β-Ga_2O_3, because it has been theoretically and experimentally reported that r-GeO_2 has ambipolar dopability [5,7], high carrier mobility [$\mu_e = 244\,\mathrm{cm^2\,V^{-1}\,s^{-1}}$ ($\perp c$) and $377\ \mathrm{cm^2\,V^{-1}\,s^{-1}}$ ($\parallel c$), $\mu_h = 27\,\mathrm{cm^2\,V^{-1}\,s^{-1}}$ ($\perp c$) and $29\,\mathrm{cm^2\,V^{-1}\,s^{-1}}$ ($\parallel c$)] [8], large breakdown field ($7.0\,\mathrm{MV\,cm^{-1}}$) [8], and higher thermal conductivity ($51\,\mathrm{Wm^{-1}\,K^{-1}}$) than β-Ga_2O_3 ($11-27\,\mathrm{Wm^{-1}\,K^{-1}}$) [9]. Moreover, bulk r-$GeO_2$ can be grown [10–12], indicating that homoepitaxial growth of r-GeO_2 will be possible in the future. Recently, growth of r-GeO_2 thin film has also been reported [13–15].

Considering the wide variety of its applications, establishment of an alloy system based on r-GeO_2, like III-V semiconductors [16], III-group nitrides [17,18], and corundum-structured oxides [19,20] is important because alloy semiconductors are bases for heterostructures contributing to various optical and electrical devices. In Figs. 1(a) and 1(b), we propose an UWBG alloy system composed of rutile-structured oxides (GeO_2-SnO_2-SiO_2 and TiO_2). Previously, r-SnO_2, which possesses a band gap of 3.56 eV [21] and an unintentional n-type conductivity, has been studied as an

*takane.hitoshi.33v@st.kyoto-u.ac.jp
†ken0710@fc.ritsumei.ac.jp

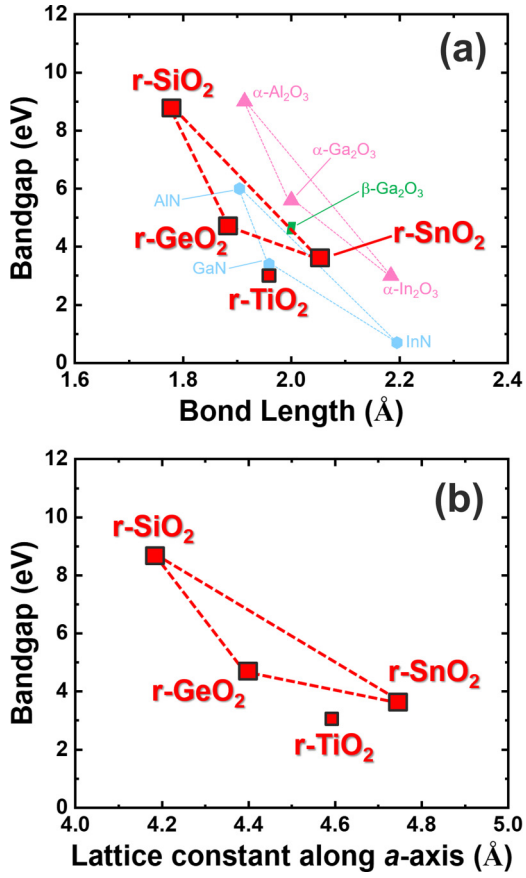

FIG. 1. (a) Relationships between band gap and bond length of a new alloy system based on rutile-structured oxides (r-GeO_2, r-SnO_2, r-SiO_2, and r-TiO_2) [4,21,27–29]. Those of conventional ones (III-group nitrides and corundum-structured oxides) and β-Ga_2O_3 are also presented [30]. (b) Relationship between band gap and lattice constant along the *a* axis of the alloy system.

attractive material for transparent conductive oxides [22], sensors [23,24], and transistors [25,26]. Also, r-SiO_2, also known as stishovite, a high-pressure phase of SiO_2, was reported to have an extremely large band gap of 8.75 eV [27]. Furthermore, r-TiO_2, with a band gap of 3.03 eV [28], shows *n*-type conductivity by Nb or Ta doping. For device-oriented research, fabrication of its alloy thin films and evaluation of their physical and structural properties are needed. Modulation of band gaps, lattice parameters, and electrical properties by changing alloy compositions is important for applications in heterostructure devices such as high electron mobility transistors and heterojunction bipolar transistors.

In this paper, we report comprehensive studies of r-$Ge_xSn_{1-x}O_2$ alloy thin films with an entire range of Ge compositions (x). Experimentally, we performed structural characterization, band-gap modulation, and the analysis of electrical properties. Along with the experiments, we carried out first-principles calculations based on density functional theory (DFT) for detailed clarification of crystal and electronic structures. Then the discussion is extended to the perspective of the GeO_2-SnO_2-SiO_2 alloy system based on the calculations.

II. EXPERIMENTAL

Here, r-$Ge_xSn_{1-x}O_2$ alloy thin films were grown on r-TiO_2 (001) substrates by a mist chemical vapor deposition (CVD) technique. Table I shows the common growth recipe for r-$Ge_xSn_{1-x}O_2$ alloy thin films. Bis [2-carboxyethylgermanium (IV)] sesquioxide (Tokyo Chemical Industry Co., Ltd.) and tin (II) chloride dihydrate (FUJIFILM Wako Pure Chemical Corp.) were used as germanium and tin precursors, respectively. We dissolved them in deionized water (H_2O) with the addition of a small amount of hydrochloric acid (HCl), which helped to solve the precursors completely. For the growth of r-$Ge_xSn_{1-x}O_2$ alloy thin films with different solidus compositions of Ge (x), we used a mixed solution of the two precursors with different Ge concentration ratios in the source solutions. The growth temperature was fixed at 725 °C, and both carrier and dilution gases were O_2 with flow rates of 3.0 and 0.5 L/min, respectively. Detailed growth conditions (growth time and concentration of Ge and Sn in the source solution) for each r-$Ge_xSn_{1-x}O_2$ alloy thin film are listed in Table II. In addition, in the mist CVD setup of this paper, we used two different quartz tubes, where the atomized source solution flows and growth reaction occurs. That is, we used quartz tubes with different lengths (50 and 75 cm) because the required times to decompose Sn and Ge precursors are different. To extend the decomposition time for the Ge precursor, we used a quartz tube with the length of 75 cm for the growth of r-$Ge_{0.96}Sn_{0.04}O_2$ and GeO_2 film, like in Ref. [14]. Note that all samples in this paper were fabricated without intentional doping. The crystal structures of r-$Ge_xSn_{1-x}O_2$ were evaluated by x-ray diffraction (XRD) measurements using Cu Kα_1 radiation with a primary Ge monochromator (Rigaku, ATX-G). The microstructure of r-$Ge_xSn_{1-x}O_2$ was observed by transmission electron microscopy (TEM) with acceleration voltage of 120 kV (FEI TECNAI F20X). The surface morphologies of the r-$Ge_xSn_{1-x}O_2$ films were observed by scanning electron microscopy (SEM) with acceleration voltage of 15 kV (Hitachi High-Tech, TM4000Plus). Energy dispersive x-ray spectroscopy (EDS) and electron backscatter diffraction (EBSD) measurements (Oxford Instruments, AZtecOne) were conducted to characterize the chemical compositions and crystallographic orientation in r-$Ge_xSn_{1-x}O_2$. Their band gaps were determined by spectroscopic ellipsometry (SE) analysis in the photon energy range of 1.5–6.5 eV (wavelength range of 190–826 nm) and at incidence angles of 70 ° (HORIBA, Ltd., UVISEL). Finally, their electrical properties were acquired by the four-probe method and Hall effect measurements with a DC magnetic field (TOYO Corp., ResiTest 8340). For the electrical measurements, we evaporated a Ti (30 nm)/Au (50 nm) electrode on the sample surface with the van der Pauw configuration.

III. CALCULATION

We performed first-principles calculations based on DFT by using the QUANTUM ESPRESSO (QE) package [31,32] and the WIEN2K code [33]. For r-$Ge_xSn_{1-x}O_2$ and r-$Ge_xSi_{1-x}O_2$ alloy modeling, we employed a generalized special quasirandom structure generated by the USPEX code [34–36] which includes 48 atoms per cell (2 × 2 × 2 primitive unit cell

TABLE I. Common growth recipe for r-$Ge_xSn_{1-x}O_2$ alloy thin films.

Ge precursor	Bis [2-carboxyethylgermanium (IV)] sesquioxide: $C_6H_{10}Ge_2O_7$
Sn precursor	Tin (II) chloride dihydrate: $SnCl_2 \cdot 2H_2O$
Solvent	$H_2O + HCl$
Substrate	r-TiO_2 (001)
Carrier gas (flow rate)	O_2 (3.0 L/min)
Dilution gas (flow rate)	O_2 (0.5 L/min)
Growth temperature	725 °C

structure) and 6 atoms per cell ($1 \times 1 \times 1$ primitive unit cell structure) for the alloys and the end members (GeO_2, SiO_2, and SnO_2), respectively. The structure optimization was performed with the Perdew-Burke-Ernzerhof (PBE) functional revised for solids [37] with the QE package. We adopted Ge, Sn, Si, and O pseudopotential files from standard solid-state pseudopotential libraries [38]. The kinetic energy cutoff for wave functions of 80 Ry and a charge density cutoff of 650 Ry, respectively, and $6 \times 6 \times 10$ and $10 \times 10 \times 16$ k points grids were used for the alloys and the end of members, respectively [39]. After structure optimization, the self-consistent calculations were performed with the WIEN2K code with 400 and 1000 k point sampling for the alloys and the end of members, respectively, PBE [40] functional and $R_aK_{\max} = 7.0$, where R_a is the smallest muffin-tin radius (here, ∼1.6–1.7 a.u. for each alloy), and $K_{\max}$ gives the magnitude of the largest K vector in the plane-wave expansion. The band gap (E_g) calculations were also performed with the Tran-Blaha modified Becke Johnson (TB-mBJ) [41,42] exchange potential implemented in WIEN2K.

To determine the natural band edge positions of r-$Ge_xSn_{1-x}O_2$ and r-$Ge_xSi_{1-x}O_2$ alloys, we used the atomic solid-state energy (SSE) scale method [43]. The scheme requires the SSE values for constitute atoms and the band gap of the system. We used the following SSE of absolute values for O, Ge, Si, and Sn: 7.96, 2.40, 2.37, and 4.26 eV, respectively [44]. The band-gap values of r-$Ge_xSn_{1-x}O_2$ and r-$Ge_xSi_{1-x}O_2$ alloys were determined from calculations via cost-effective TB-mBJ results.

IV. RESULTS AND DISCUSSIONS

A. Structural analysis by XRD and TEM

Figures 2(a) and 2(b) show XRD symmetric $2\theta/\omega$ scan profiles of r-$Ge_xSn_{1-x}O_2$ alloy films on r-TiO_2 (001) substrate in wide (20–90°) and narrow (54–68°) ranges, respectively. The peaks of r-$Ge_xSn_{1-x}O_2$ 002 diffraction and r-TiO_2 002 diffraction are visible, indicating that (001)-oriented r-$Ge_xSn_{1-x}O_2$ alloy films were grown on r-TiO_2 (001) substrates. Using the EDS described in detail later, Ge compositions (x) in each film were found to be 0.00, 0.41, 0.57, 0.66, 0.70, 0.96, and 1.00. The EDS compositions were calibrated by using standard samples, where metallic Sn and Ge powder were mixed with different compositions. It should be noted that the diffraction peak at ∼30° in the profile for $x = 0.70$ is attributed to a forbidden 001 diffraction by the film or substrate.

Figure 2(c) presents the XRD (301) Φ scan profile of the r-$Ge_{0.57}Sn_{0.43}O_2$ film on r-TiO_2 substrate. For the r-$Ge_{0.57}Sn_{0.43}O_2$ film, peaks appear at the same fourfold rotational angle Φ as (001) r-TiO_2 substrate with 90° interval. This suggests that (001)-oriented r-GeO_2 film was epitaxially grown on (001) TiO_2 substrate without rotational domains.

To evaluate crystalline quality of the alloy films, XRD symmetric rocking curve (RC) ω scan measurements were conducted. The RC-full width at half maximums (RC-FWHMs) of the 002 diffraction and thicknesses of the r-$Ge_xSn_{1-x}O_2$ alloy films as a function of Ge compositions (x) are shown in Fig. 3. The film thicknesses were obtained by SE analysis. The values of thickness of the films with $x = 0.70$ and 1.00 were excluded because SE analysis could not be applied for the two films as described below, although their thicknesses were estimated to be ∼350 nm ($x = 0.70$) from the growth rate of $x = 0.66$ because these two compositions ($x = 0.70$ and 0.66) are almost the same and 500–1000 nm ($x = 1.00$) due to the growth rate reported in Ref. [14]. First, it should be noted that the RC-FWHMs of the end members of the alloys are ∼100 arcsec ($x = 0.00$) and ∼500 arcsec ($x = 1.00$), which are comparable with or slightly smaller than those of previously reported r-SnO_2 and r-GeO_2 films on TiO_2 (001) substrates [14,45]. As shown in Fig. 3, the RC-FWHMs sharply increase for $x = 0.70$ and 0.96, which means that crystallinities of r-$Ge_xSn_{1-x}O_2$ degrade due to higher inclusion level of Ge as well as alloying compared with the end members, that is, SnO_2 and GeO_2. In fact, Ge-rich r-$Ge_xSn_{1-x}O_2$ films ($x > 0.5$) have not been demonstrated,

TABLE II. Detailed growth conditions for each of the r-$Ge_xSn_{1-x}O_2$ alloy thin films.

Ge compositions (x)	Growth time (min)	$C_6H_{10}Ge_2O_7$ in solution (m mol/L)	$SnCl_2 \cdot 2H_2O$ in solution (m mol/L)	Quartz tube length (cm)
0.00	30	0	50	50
0.41	15	16	25	50
0.57	15	16	16	50
0.66	15	13	6	50
0.70	60	5	2.5	50
0.96	30	10	2.5	75
1.00	25	10	0	75

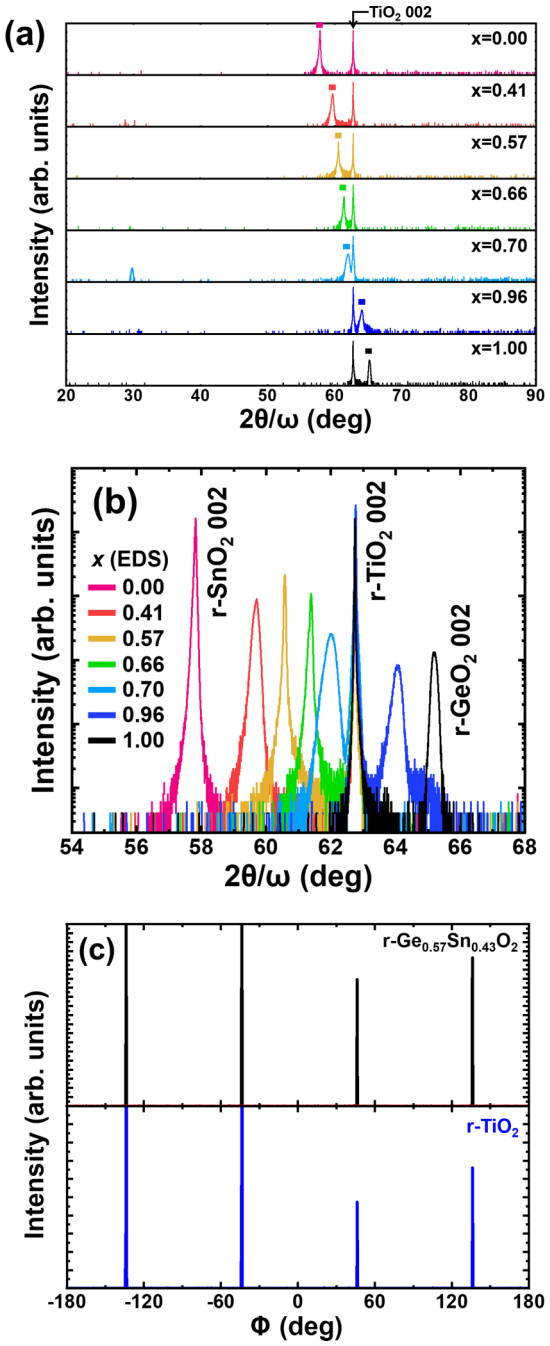

FIG. 2. X-ray diffraction (XRD) symmetric $2\theta/\omega$ scan profiles of r-$Ge_xSn_{1-x}O_2$ alloy thin films on r-TiO_2 (001) substrates in (a) a wide and (b) a narrow range. The compositions of Ge (x) in the thin films were determined by the energy dispersive x-ray spectroscopy (EDS). The solid squares in (a) represent 002 diffraction peaks of r-$Ge_xSn_{1-x}O_2$ alloy thin films. (c) XRD (301) Φ scan profile of r-$Ge_{0.57}Sn_{0.43}O_2$ alloy thin films (black line) and r-TiO_2 substrate (blue line).

and r-GeO_2 was reported to show fluctuation in its crystallinity [14,15,46], suggesting that Ge-rich r-$Ge_xSn_{1-x}O_2$ and r-GeO_2 have poor stabilities. However, we believe that it is possible to improve the stability by preparing the compounds under optimized conditions. On the other hand, for $x = 0.57$ and 0.66, although the alloy films include relatively

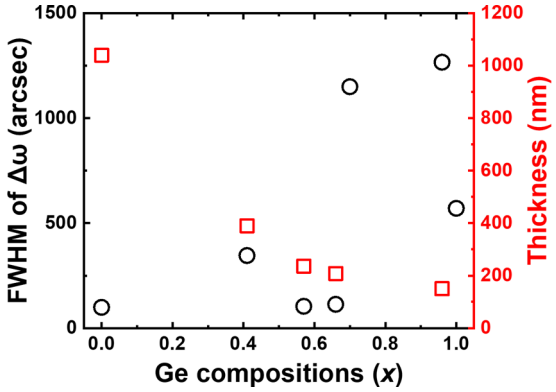

FIG. 3. X-ray diffraction (XRD) symmetric rocking curve (RC)-full width at half maxima (FWHMs; black balls) and thicknesses obtained by the spectroscopic ellipsometry (SE; red squares) of r-$Ge_xSn_{1-x}O_2$ alloy films as a function of Ge compositions (x). The thicknesses films with $x = 0.70$ and 1.00 are excluded.

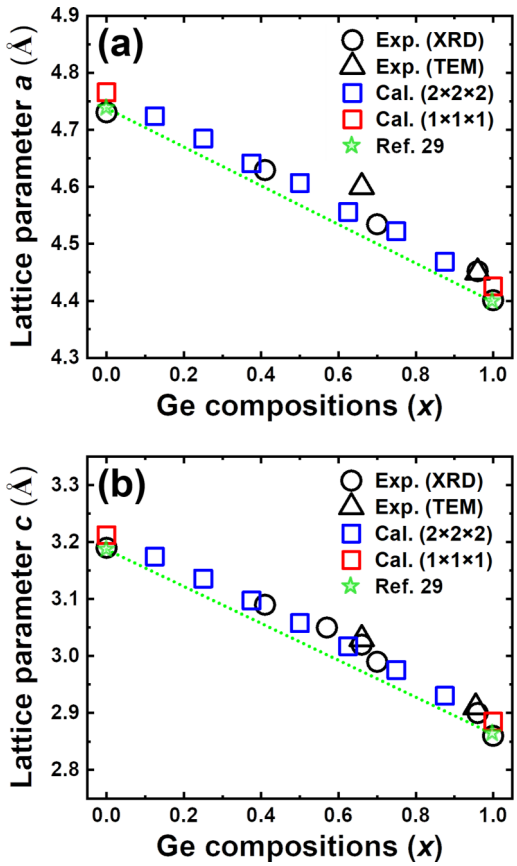

FIG. 4. Experimentally obtained and calculated lattice constants of r-$Ge_xSn_{1-x}O_2$ alloy thin films along (a) the a axis and (b) c axis as a function of Ge compositions (x). Black circle and triangles, blue and red squares represent experimental values obtained by x-ray diffraction (XRD) and transmission electron microscopy (TEM) calculated values with supercells of $2 \times 2 \times 2$ and $1 \times 1 \times 1$, respectively. Green stars and dashed lines represent values of lattice parameters cited from Ref. [29] and those expected by the Vegard's law based on the referred values.

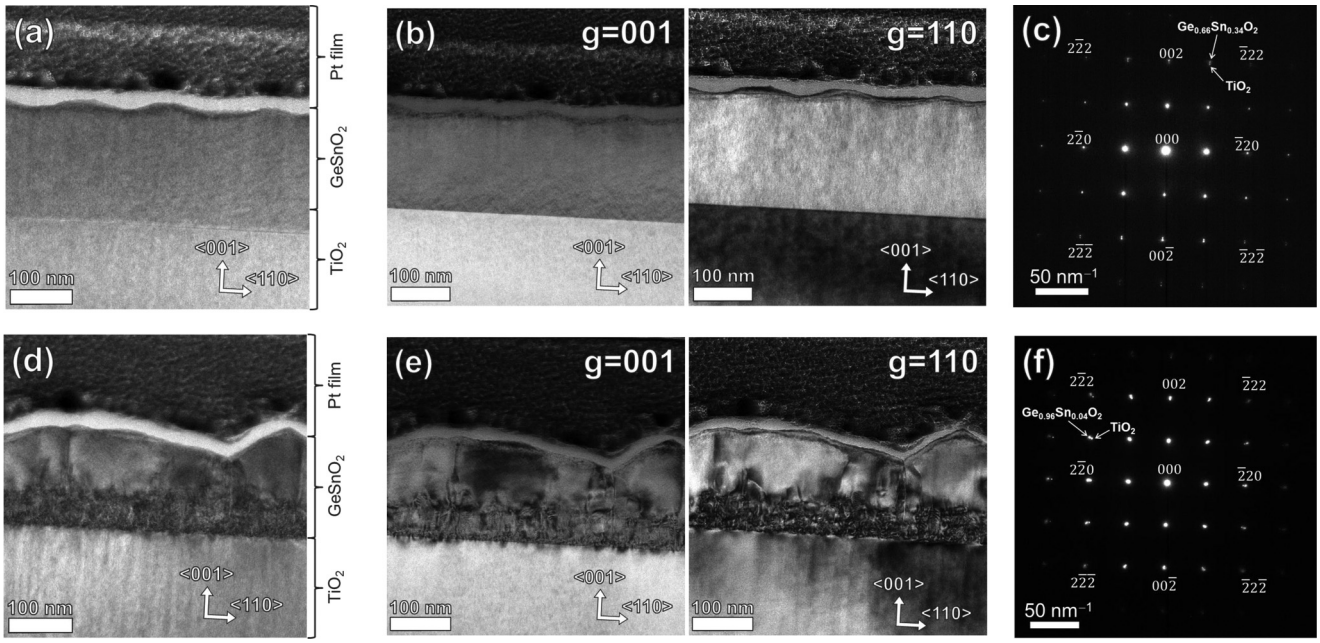

FIG. 5. Cross-sectional transmission electron microscopy (TEM) images at the (a) r-$Ge_{0.66}Sn_{0.34}O_2$/r-TiO_2 and (d) r-$Ge_{0.96}Sn_{0.04}O_2$/r-TiO_2 interface. Cross-sectional TEM images (bright-field) in two-beam diffraction condition with $\mathbf{g} = 001$ and 110 at the (b) r-$Ge_{0.66}Sn_{0.34}O_2$/r-TiO_2 and (e) r-$Ge_{0.96}Sn_{0.04}O_2$/r-TiO_2 interface. Selected area electron diffraction (SAED) patterns at the (c) r-$Ge_{0.66}Sn_{0.34}O_2$/r-TiO_2 and (f) r-$Ge_{0.96}Sn_{0.04}O_2$/r-TiO_2 interface. All the TEM images were viewed along the ⟨110⟩ zone axis.

higher levels of Ge, the RC-FWHMs are relatively small. As shown in Fig. 4(a), which is described in detail later, the calculated lattice constant along the a axis of r-$Ge_xSn_{1-x}O_2$ with Ge compositions of 0.5–0.6 is found to be close to that of r-TiO_2 ($a_{TiO} = 4.5941$ Å) [29]. Therefore, for $x = 0.57$ and 0.66, it is considered that the decreased lattice mismatches around the midrange of the Ge composition lead to the small FWHMs of ∼100 arcsec.

Then we conducted the TEM observations for the r-$Ge_xSn_{1-x}O_2$ of $x = 0.66$ and 0.96. Figures 5(a) and 5(d) indicate cross-sectional TEM images at the r-$Ge_{0.66}Sn_{0.34}O_2$/r-TiO_2 and r-$Ge_{0.96}Sn_{0.04}O_2$/r-TiO_2 interfaces, respectively. Figures 5(b) and 5(e) show cross-sectional TEM images (bright-field) in the two-beam diffraction condition with g = 001 and 110 at the r-$Ge_{0.66}Sn_{0.34}O_2$/r-TiO_2 and r-$Ge_{0.96}Sn_{0.04}O_2$/r-TiO_2 interfaces, respectively. Note that all the TEM images were viewed along the ⟨110⟩ zone axis. Selected area electron diffraction (SAED) patterns at the r-$Ge_{0.66}Sn_{0.34}O_2$/r-TiO_2 and r-$Ge_{0.96}Sn_{0.04}O_2$/r-TiO_2 interfaces are illustrated in Figs. 5(c) and 5(f), respectively. Figures 5(a) and 5(b) suggest that there are few dislocations with components of Burgers vector $\mathbf{b} = \langle 001 \rangle$ and ⟨110⟩ in the film with $x = 0.66$. In the SAED pattern of $x = 0.66$ in Fig. 5(c), spots originating from the film are situated outside of and at almost the same positions as the r-TiO_2 spots along the ⟨001⟩ and ⟨110⟩ axes, respectively. Such positions of the spots are consistent with the lattice mismatch along the a axis decreasing and the RC-FWHM being relatively low. Given the lattice mismatch along the a axis described above, the film thickness (208 nm) of the r-$Ge_{0.66}Sn_{0.34}O_2$ film on r-TiO_2, and almost the same positions of their SAED spots along the ⟨110⟩ axis, it is considered that the in-plane lattice relaxation did not occur, or the relaxation ratio is small in r-$Ge_{0.66}Sn_{0.34}O_2$/r-TiO_2. Therefore, less dislocation density in the film with $x = 0.66$ may be attributed to such decreased lattice mismatch and the resultant zero or small relaxation ratio. However, the critical thickness depends not only on lattice mismatches but also on the direction and size of Burgers vectors, slip plane of misfit dislocations, and so on. Thus, further studies and discussions are needed. On the other hand, as shown in Figs. 5(d) and 5(e), there seem to be many dislocations in the region near the interface in the film. The dislocation density in the region near the interface is estimated to be $> 10^{10}\,cm^{-2}$ based on the method of Ham [47]. The dislocations are considered to annihilate and/or coalesce above the region near the interface, and there seem to be much fewer dislocations in the region near the surface than the region near the interface. Furthermore, in Fig. 5(e), the two-beam diffraction condition observation with both $\mathbf{g} = 001$ and 110 shows a lot of dislocations, indicating that both dislocations with screw ($\mathbf{b} = \langle 001 \rangle$) and edge ($\mathbf{b} = \langle 110 \rangle$) components and/or mixed dislocations are present in the region near the interface in the r-$Ge_{0.96}Sn_{0.04}O_2$ film. In this paper, although the r-GeO_2 film was not observed by TEM, the RC-FWHM of the r-GeO_2 film in this paper is compatible with the values reported in Refs. [14,46]. Thus, it is considered that the r-GeO_2 film in this paper possesses the same number of dislocations as reported in Refs. [14,46].

Here, the lattice constants of the r-$Ge_xSn_{1-x}O_2$ alloy films were obtained by XRD and TEM. Those along the a and c axes were obtained from 220 diffraction peaks of in-plane $2\theta\chi/\Phi$ scans and 002 diffraction peaks of the symmetric $2\theta/\omega$ scans, respectively. Note that the a-axis lengths of $x = 0.57$ and 0.66 cannot be acquired by the $2\theta\chi/\Phi$ scans because their values are relatively like that of r-TiO_2, and it is

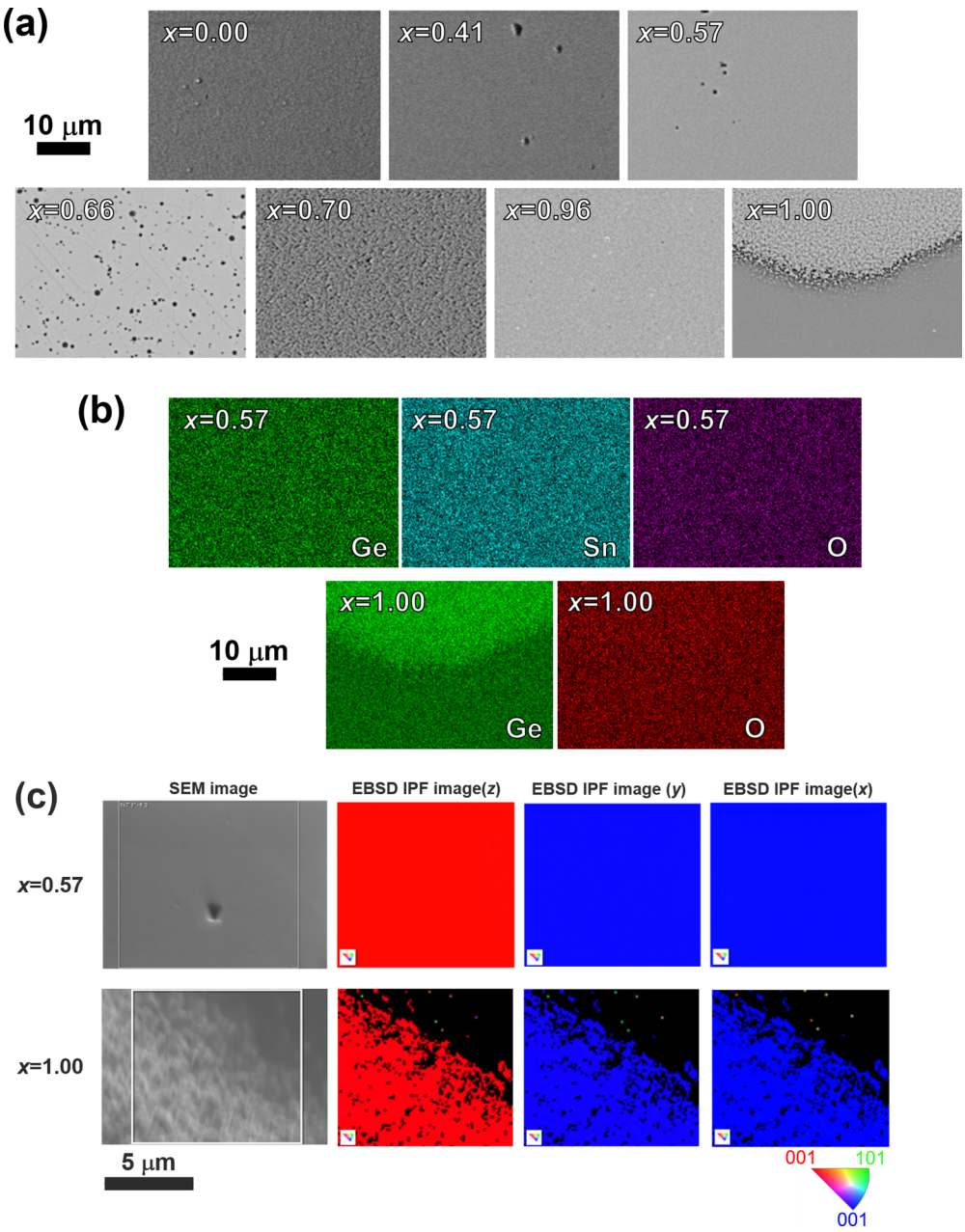

FIG. 6. (a) Plane-view scanning electron microscopy (SEM) images of r-$Ge_xSn_{1-x}O_2$ films with $x = 0.00$, 0.41, 0.57, 0.66, 0.70, 0.96, and 1.00. (b) Plane-view energy dispersive x-ray spectroscopy (EDS) mapping of r-$Ge_xSn_{1-x}O_2$ films with $x = 0.57$ and 1.00. The observed areas are consistent with the SEM images in (a). (c) Plane-view electron backscatter diffraction (EBSD) mapping of r-$Ge_xSn_{1-x}O_2$ films with $x = 0.57$ and 1.00. The observed areas are shown by white squares in the SEM (left).

difficult to identify the 220 diffraction peaks originated from the films. For $x = 0.66$ and 0.96, the lattice constants were also estimated from the SAED pattern shown in Figs. 5(c) and 5(f). We corrected the experimental values based on the lattice parameters of r-TiO_2 ($a_{TiO} = 4.5941$ Å and $c_{TiO} = 2.9589$ Å) [29] in the calculations. Figures 4(a) and 4(b) depict the experimentally obtained and calculated lattice constants along the a and c axes, respectively, as a function of Ge compositions (x), as well as the those previously reported for the end members [29]. It is confirmed that the lattice constants along both the a and c axes decrease as Ge compositions (x) increase. Additionally, as presented in both Figs. 4(a) and 4(b), this trend of the experimental values is very consistent with not only those derived by DFT calculations but also those expected by Vegard's law based on the referred values (green dashed lines).

B. Surface, chemical, and crystalline characterization by SEM, EDS, and EBSD

Figure 6(a) illustrates plane-view SEM images of r-$Ge_xSn_{1-x}O_2$ films with $x = 0.00$, 0.41, 0.57, 0.66, 0.70, 0.96, and 1.00. As shown in Fig. 6(a), there seem to be some pits or something on the surface of the films with $x = 0.57$ and 0.66, and the surface of the film with $x = 0.70$ seems rough.

Additionally, for $x = 1.00$, phase separation can be seen, that is, one surface area is rough, and the other is smooth.

Figure 6(b) exhibits plane-view EDS mappings of r-$Ge_xSn_{1-x}O_2$ films with $x = 0.57$ and 1.00. The observed areas are the same as the SEM images in Fig. 6(a). For $x = 0.57$, it is confirmed that Ge, Sn, and O are uniformly distributed, and there is no remarkable phase separation area in the film. It should be noted that no other elements were detected except for Ti, which is a component of the substrates used in this paper, and Ti was detected because the penetration depth of the incidence electrons was longer than the film thickness, and the incidence electrons reached the substrate. This uniform distribution of elements with no phase separation was also observed for the films with $x = 0.00, 0.41$, 0.66, 0.70, and 0.96. On the other hand, for $x = 1.00$, the color strength of Ge is uniform in each area (the rough surface area and the smooth surface area) but different from each other. This is because the r-$Ge_xSn_{1-x}O_2$ with $x = 1.00$ shows fluctuation in its thickness, as reported in Ref. [46], and the integral intensity for Ge becomes brighter in the thicker area. No other elements except for Ge, O, and Ti were detected for $x = 1.00$.

To analyze the crystallographic orientation of r-$Ge_xSn_{1-x}O_2$ films and phase separation in the r-$Ge_xSn_{1-x}O_2$ with $x = 1.00$, the EBSD measurements were conducted. In the measurements, the coordinates of the equipment were set as follows: the z axis of the equipment is parallel to the $\langle 001 \rangle$ axis of the TiO_2 substrate, and the x and y axes of the equipment are parallel to the equivalent $\langle 110 \rangle$ axes of the TiO_2 substrate. In this paper, to analyze the measured EBSD patterns and detect crystallographic orientations of the films, we used crystallographic data including chemical compositions, space group, cell parameters, and atom coordinates of r-SnO_2 and r-GeO_2 [29] for the films with $x = 0.00$ and 1.00, respectively. For the analysis of the EBSD patterns of the films with $x = 0.41$, 0.57, 0.66, 0.70, and 0.96, we prepared original data, where chemical compositions are set to x values, space group and atom coordinates are the same as conventional rutile structure, and cell parameters are estimated by using Vegard's law. Figure 6(c) exhibits the EBSD inverse pole figure (IPF) maps along the x, y, and z axes. The observed areas are shown by the SEM images on the left-hand side. The color map indicating plane orientations is also illustrated in the bottom right. For $x = 0.57$, the EBSD IPF map along the z axis and those along the x and y axes correspond well to (001) and (110) orientations, respectively, of the rutile structure, indicating that both the out-of-plane and in-plane orientations of r-$Ge_xSn_{1-x}O_2$ with $x = 0.57$ and r-TiO_2 substrate are consistent with each other, and the film are epitaxially grown on the substrate. The same results were obtained for $x = 0.00$, 0.41, 0.66, 0.70, and 0.96. On the contrary, for $x = 1.00$, although the same results are observed and the same out-of-plane and in-plane orientations between the film and substrate were confirmed in the rough surface area, the EBSD IPF maps along all the axes show almost no orientation of the rutile structure in the smooth surface area. This result suggests that r-$Ge_xSn_{1-x}O_2$ with $x = 1.00$ shows fluctuation in its crystallinity, as reported in Ref. [46], as well as in its thickness. The black points in the well-crystallized region are attributed to multiple scattering of diffraction electrons by its rough surface.

C. Modulation of band gaps and electronic structures

To estimate band gaps of the r-$Ge_xSn_{1-x}O_2$ alloy thin films, we performed SE analyses for the films with $x = 0.00$, 0.41, 0.57, 0.66, and 0.96. In the analysis, we used the Tauc-Lorenz (T-L) dispersion formula [48,49] as a fitting model for ellipsometric parameters (Δ, Ψ), which are related to the complex ratio of the Fresnel reflection coefficients as $\rho = \tan\Psi \exp(i\Delta)$. For $x = 0.70$, 1.00, measured ellipsometric parameters cannot be well fitted by the T-L model due to the rough surface ($x = 0.70$, 1.00). Additionally, for $x = 1.00$, the ill fitting is also affected by the fluctuation in its thickness and crystallinity in-plane, as described above and in Ref. [46].

In this paper, the band gaps were determined using a Tauc plot. Nagasawa and Shinomiya [50,51] reported that the band gap of rutile-structured SnO_2 was direct forbidden, and the band gaps have been acquired assuming the direct-forbidden transitions for r-SnO_2 and r-GeO_2 [4,21]. Thus, we also assumed the direct-forbidden transition for the r-$GeSnO_2$ alloys in this paper. Assuming direct-forbidden transition, the absorption coefficient (α) and the band gap (E_g) are described as follows [52,53]:

$$(\alpha h\nu)^{1/n} = A(h\nu - E_g),\ n = \tfrac{3}{2}, \tag{1}$$

where $h\nu$ is incidence photon energy, and A is a constant. The absorption coefficient is represented by $\alpha = 4\pi k/\lambda$ using the derived extinction coefficient k and the incidence wavelength λ. Figure 7(a) shows the relationships between $(\alpha h\nu)^{2/3}$ and the incidence photon energy. The band gaps were estimated from the intersection of the extrapolated straight line, which is the liner fitting of the $(\alpha h\nu)^{2/3}$-$h\nu$ plots, with the photon energy axis, and found to be 3.81 ($x = 0.00$), 3.95 ($x = 0.41$), 3.98 ($x = 0.57$), 4.02 ($x = 0.66$), and 4.44 eV ($x = 0.96$). The obtained band gaps of r-$Ge_xSn_{1-x}O_2$ ($x \leqslant 0.96$) as a function of the Ge compositions (x) are shown in Fig. 7(b). For $x = 1.00$, we adopted the value of bulk r-GeO_2 reported in Ref. [4] (blue triangle) because we could not estimate its band gap from the SE analysis for the present thin film. It is confirmed that the band-gap value of r-$Ge_xSn_{1-x}O_2$ increases as Ge composition increases in a Ge composition range of $0.00 \leqslant x \leqslant 0.96$. In addition, like typical alloy semiconductors, there seems to be band-gap bowing in r-$Ge_xSn_{1-x}O_2$ alloys. Using a bowing parameter (b), which is a degree of deviations of the band-gap values of the alloy from the linear interpolation of the values of endpoint constituents, band gaps of r-$Ge_xSn_{1-x}O_2$ [$E_g^{\mathrm{GeSnO}}(x)$] can be expressed as

$$E_g^{\mathrm{GeSnO}}(x) = xE_g^{\mathrm{GeO}} + (1-x)E_g^{\mathrm{SnO}} - bx(1-x), \tag{2}$$

where E_g^{GeO} and E_g^{SnO} are the band gaps of r-GeO_2 and r-SnO_2, which were set at 4.68 eV [4] and 3.81 eV, respectively. By the curve fitting shown in Fig. 4(b), the bowing parameter of the alloy system was estimated to be 1.2 eV.

To deeply analyze the shift of band gaps and electronic structures in r-$Ge_xSn_{1-x}O_2$ alloys accompanying the Ge compositions change, we used first-principles calculations. First, we compared the experimental and calculated band-gap values. It is a common phenomenon that first-principles calculations underestimate band-gap values unless using frameworks with high cost such as hybrid functionals

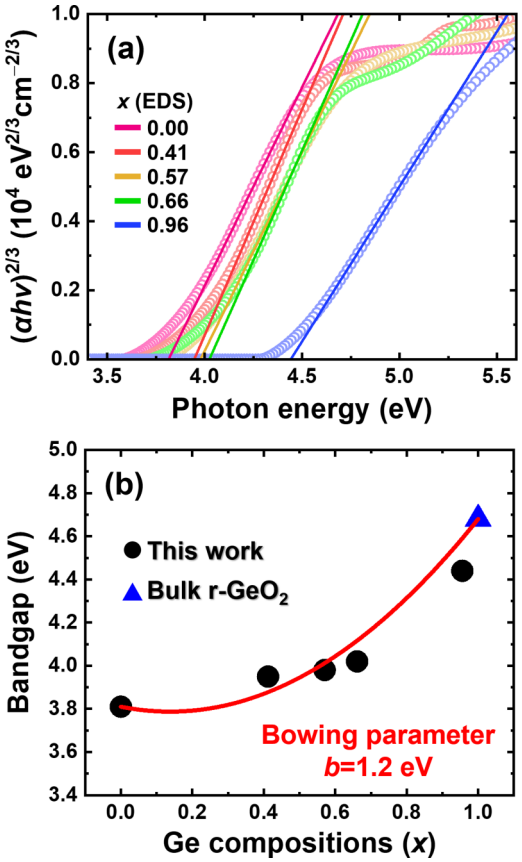

FIG. 7. (a) Relationships between $(\alpha h\nu)^{2/3}$ and the incidence photon energy in r-$Ge_xSn_{1-x}O_2$ alloy thin films with $x = 0.00$, 0.41, 0.57, 0.66, and 0.96 (blank circles). The solid lines represent the linear fitting of the $(\alpha h\nu)^{2/3}$-$h\nu$ plots. The band gaps were estimated from the intersection with the photon energy axes. (b) The band gaps of r-$Ge_xSn_{1-x}O_2$ alloy thin films obtained by the spectroscopic ellipsometry (SE) measurements and the Tauc plots for the direct-forbidden transitions as a function of Ge compositions (black balls) and that of bulk r-GeO_2 (blue triangle) [4]. The bowing parameter b was found to be 1.2 eV by curve fitting (red line).

[54–56] or GW approximation [57,58], which originates from the lack of derivative discontinuity and spurious self-interaction. However, it is unrealistic to use such accurate but high-cost methods of calculations for alloys treated in this paper because a large cell is needed to accurately calculate the electronic structure of alloys containing different types of elements with a wide range of compositions. Therefore, we used the TB-mBJ (Meta-GGA) method which relatively balances the cost and accuracy as described above. Calculations with a heavy cost gave values (PBE0: 3.8 eV [7], G_0W_0@HSE06 : 3.89 eV [59]) for SnO_2 which are very consistent with our experimentally obtained value (3.81 eV). To correct the underestimation of calculated band-gap values, we compared experimental and calculated ΔE_g. Here, we define each ΔE_g as $\Delta E_g = E_g$-E_g^{SnO}, where E_g and E_g^{SnO} are the band-gap values of r-$Ge_xSn_{1-x}O_2$ alloys and r-SnO_2, respectively. The experimental and calculated E_g^{SnO} are 3.81 and 3.48 eV, respectively. Figure 8(a) presents experimental and calculated ΔE_g as a function of Ge compositions (x). From Fig. 8(a), it can be said that the band-gap modulation with

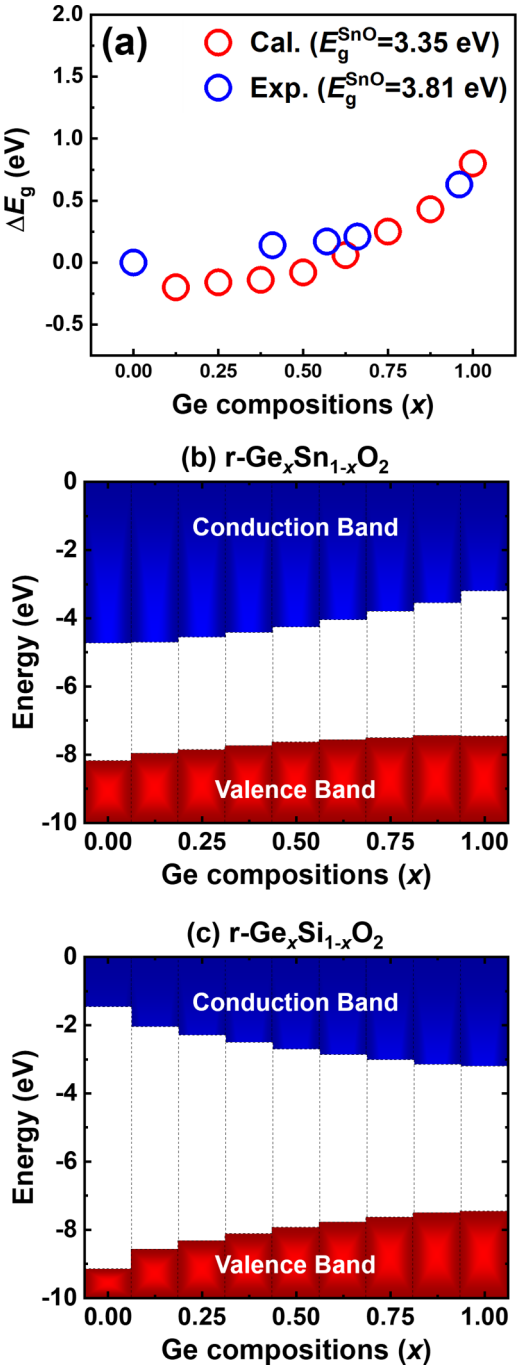

FIG. 8. (a) Experimental (blue circle) and calculated (red circle) ΔE_g as a function of Ge compositions (x). The band-gap values for r-SnO_2 (E_g^{SnO}) of 3.81 and 3.35 eV, respectively, and each ΔE_g is defined as $\Delta E_g = E_g$-E_g^{SnO}, where E_g are band gaps of r-$Ge_xSn_{1-x}O_2$ alloy films. (b) Calculated natural band alignment of r-$Ge_xSn_{1-x}O_2$ alloys as a function of Ge compositions. (c) Calculated natural band alignment of r-$Ge_xSi_{1-x}O_2$ alloys as a function of Ge compositions. The energy values are referenced to the vacuum level in both (b) and (c).

Ge compositions experimentally obtained is supported by the calculations.

Then we present a calculated natural band alignment of r-$Ge_xSn_{1-x}O_2$ alloys as a function of Ge compositions (x) in

Fig. 8(b). The energy values are referenced to the vacuum level. In Fig. 8(b), it is estimated that both the conduction band minimum (CBM) and valence band maximum (VBM) become shallow as Ge compositions (x) increase. The heterojunction of r-$Ge_xSn_{1-x}O_2$ with different compositions was found to be a staggered gap (type-II) in almost an entire range of Ge compositions (x). The trend of the VBM in r-$Ge_xSn_{1-x}O_2$ alloys with an increase in Ge compositions (x) agrees with the shallowing of the VBM from r-SnO_2 to r-GeO_2 reported in Refs. [5,7], though the VBM offset of r-SnO_2/r-GeO_2 is relatively smaller than those in Refs. [5,7] due to our calculation with lower cost. This trend of shallowing of the VBM is a key for achievement of p-type doping in r-GeO_2 (and highly Ge-rich r-$Ge_xSn_{1-x}O_2$ alloys), as mentioned just below. The Fermi level lies within the n- and p-type Fermi pinning energies ($E^n_{\rm pin}$ and $E^p_{\rm pin}$, respectively), which are roughly universal for materials with a similar chemical group, such as III-V and II-VI materials and metal oxides [60–64]. (For oxide semiconductors, $E^n_{\rm pin}$ and $E^p_{\rm pin}$ lie at ∼3.5 and 6.5 eV below the vacuum level, respectively [64].) In other words, if the Fermi level rises above $E^n_{\rm pin}$ or drops below $E^p_{\rm pin}$, compensation defects will spontaneously form, pinning the Fermi level at $E^n_{\rm pin}$ and $E^p_{\rm pin}$. Consequently, the shallower the VBM becomes, the higher the efficiency of p-type doping would be. Furthermore, intrinsic properties of given materials for doping efficiencies have also been similarly discussed in terms of the amphoteric defect model and Fermi-level stabilization energy [65–68]. Thus, our result, which indicates the trend of shallowing of the VBM with an increase in Ge compositions, encourages realization of p-type doping in r-GeO_2 (and highly Ge-rich r-$Ge_xSn_{1-x}O_2$ alloys) and should contribute to further discussions and challenges for fabrication of p-type oxide semiconductors, though the calculated VBM of r-GeO_2 seems deeper than the $E^p_{\rm pin}$ (6.5 eV below the vacuum level) due to our calculation with lower cost.

At the end of this section, the natural band alignment of r-$Ge_xSi_{1-x}O_2$ alloys is shown in Fig. 8(c). It is confirmed that, as Si compositions increase, the band gap of r-$Ge_xSi_{1-x}O_2$ alloys sharply increase (4.28–7.70 eV). At the same time, the CBM becomes shallower, and the VBM becomes deeper with an increase in Si compositions, indicating that the interface of r-$Ge_xSi_{1-x}O_2$ with different alloy compositions is type I. In addition, as found in Fig. 8(c), r-SiO_2 and Si-rich r-$Ge_xSi_{1-x}O_2$ alloys have shallow CBM and deep VBM, suggesting that it may be extremely difficult to achieve both n- and p-type conduction from the viewpoint of the Fermi pinning energy and/or the Fermi-level stabilization energy, as mentioned above. However, these large CBM and VBM offsets are preferable to use as blocking layers of other rutile-structured devices.

D. Electrical properties

We investigated electrical properties of r-$Ge_xSn_{1-x}O_2$ alloy films ($x = 0.00$, 0.41, 0.57, 0.66, 0.70, and 0.96) by the four-probe method and Hall effect measurements with the van der Pauw configuration. As described in the experimental section, all the samples in this paper were grown without intentional doping. We excluded the sample with $x = 1.00$ because it is difficult to measure the accurate property of crystallized r-GeO_2 due to fluctuation in its crystallinity. Figure 9(a) shows the resistivities of r-$Ge_xSn_{1-x}O_2$ measured by the four-probe method as a function of Ge compositions (x), indicating that r-$Ge_xSn_{1-x}O_2$ with $x \leqslant 0.96$ shows relatively high conductivity without intentional doping. Figures 9(b) and 9(c) exhibit the carrier concentrations and mobilities of r-$Ge_xSn_{1-x}O_2$ films determined by Hall effect measurements as a function of Ge compositions (x). Hall effect measurements with a DC magnetic field demonstrate that r-$Ge_xSn_{1-x}O_2$ with $x \leqslant 0.57$ manifests n-type conductivity. To further confirm the carrier type and whether a single carrier model applies, we also measured the Hall voltages under varied magnetic fields for r-$Ge_xSn_{1-x}O_2$ with $x = 0.00$, 0.41, and 0.57. As shown in Fig. 9(d), the Hall voltages are negatively proportional to the applied magnetic fields for r-$Ge_{0.57}Sn_{0.43}O_2$, which confirms n-type conductivity and availability of a single-carrier model. The negative linear dependences of the Hall voltages on the applied magnetic fields were also observed for films with $x = 0.00$, 0.41.

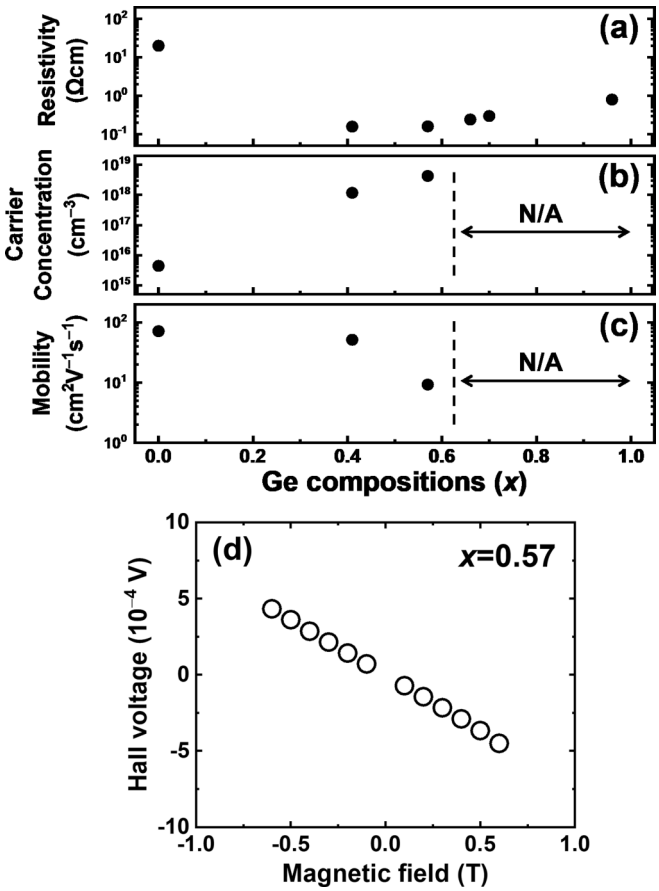

FIG. 9. (a) Resistivities, (b) carrier concentrations, and (c) mobilities of r-$Ge_xSn_{1-x}O_2$ alloy thin films as a function of Ge compositions (x). (d) Relationship between the Hall voltages and applied magnetic fields of r-$Ge_{0.57}Sn_{0.43}O_2$ alloy thin film.

Hydrogen-related defects including interstitial hydrogen (H_i) and hydrogen on an oxygen site (H_O) are considered one of the dominant carrier (electron) sources because it is theoretically reported that both H_i^+ and H_O^+ have low formation energy and act as shallow donors in both r-SnO_2 [69,70] and

r-GeO_2 [5]. In addition, muon spin resonance spectroscopy suggests that hydrogen forms a shallow-donor center in SnO_2 [71]. Hydrogen can be supplied by H_2O, which is carried to the reaction area as the source solution in the mist CVD method. As indicated in Fig. 9(b), the carrier concentrations increase as Ge compositions increase, suggesting that the hydrogen-related defects may increase by incorporating Ge in r-SnO_2. In addition, Fig. 9(c) shows that the mobilities decrease as Ge compositions increase, which is probably because the alloy scattering, due to a disorder potential arising from the random distribution of the constituent atoms among the available lattice sites, is remarkable in the midrange of the alloy composition [72–74]. Moreover, inclusion of pits for $x = 0.57$, as found in Fig. 6(a), restrict carrier mobility. On the other hand, it should be noted that oxygen vacancy (V_O) is theoretically reported to act as a deep donor in both r-SnO_2 [70] and r-GeO_2 [5]; thus, V_O may not be a main carrier source, which is in contradiction with the conventional attribution of *n*-type conductivity in SnO_2 to V_O. However, it is difficult to determine the exact origin of a main carrier source in the present thin films. Thus, further studies are needed to specify it. For $x = 0.66$, 0.70, and 0.96, the carrier type, carrier concentration, and mobility cannot be identified by Hall effect measurements owing to scattered data, probably because carrier mobility is so low that the Hall voltages are not accurately obtained. This is probably because the alloy scattering is significantly effective, the film with $x = 0.66$ includes some pits, and/or the crystallinity of the films with $x = 0.70$ and 0.96 is drastically degraded, as mentioned above. Nevertheless, it should be noted that the films with $x \leqslant 0.57$ exhibit *n*-type conductivity, and those with $x = 0.66$, 0.70, and 0.96 manifest resistivities $<1\ \Omega$ cm, though the electrical properties become inferior with increase Ge compositions.

Finally, in this paper, we only prepared undoped r-$Ge_xSn_{1-x}O_2$ alloy films; therefore, relationships between doping and electrical properties in the alloy should be investigated in the future. From this point of view, several experimental and theoretical reports on binary r-SnO_2 and r-GeO_2 suggest that F [5,75], Sb [5,76], As [5], and Ta [45]; and Al [5], Ga [9], and In [5] are considered to be candidates for *n*- and *p*-type dopants, respectively. Chae *et al.* [5] proposed that codoping acceptors with hydrogen and subsequent annealing like GaN with Mg was one of the strategies for achieving *p*-type doping. Thus, both experimental and theoretical studies are needed.

V. CONCLUSIONS

In this paper, we proposed an UWBG alloy system based on rutile-structured oxides (GeO_2-SnO_2-SiO_2) and reported results of experimental investigations and first-principles calculations. Experimentally, we fabricated (001)-oriented r-$Ge_xSn_{1-x}O_2$ alloy thin films on r-TiO_2 (001) substrates with an entire range of Ge compositions (x) by the mist CVD technique. From the structural characterizations including XRD, EDS, and EBSD, fabricated r-$Ge_xSn_{1-x}O_2$ alloy films with $x \leqslant 0.96$ and the well-crystallized area in the film with $x = 1.00$ have uniform distribution of Ge, Sn, and O and the rutile-structure with the same in-plane and out-of-plane orientation as r-TiO_2 substrates. The TEM observations display few dislocations in r-$Ge_{0.66}Sn_{0.34}O_2$ probably because the in-plane lattice mismatch is relatively small. On the other hand, there are a lot of both edge and screw or mixed dislocations near the film/substrate interface in r-$Ge_{0.96}Sn_{0.04}O_2$. The lattice constants along both the *a* and *c* axes decrease with an increase in Ge compositions. The values of lattice constants and their compositional dependence are in good agreement with those obtained by our calculations. SE analysis demonstrates that their band gaps increase as Ge compositions increase (3.81–4.44 eV), with a bowing parameter of 1.2 eV. The trend of experimentally determined band gaps of the r-$Ge_xSn_{1-x}O_2$ alloy films is generally consistent with that of the calculations. Moreover, we presented the calculated natural band alignments of r-$Ge_xSn_{1-x}O_2$ and r-$Ge_xSi_{1-x}O_2$ alloys. The results indicate that the shallowing of the VBM in r-$Ge_xSn_{1-x}O_2$ takes place as the increase in Ge compositions, which is a key for achieving *p*-type conduction in r-GeO_2 and Ge-rich r-$Ge_xSn_{1-x}O_2$. It was also found that the band gaps of r-$Ge_xSi_{1-x}O_2$ alloys sharply increase with the CBM shallowing and the VBM deepening as Si compositions increase, suggesting that it is preferable to use r-SiO_2 and Si-rich r-$Ge_xSi_{1-x}O_2$ as blocking layers of other rutile-structured devices. Our measurements of electrical properties indicate that r-$Ge_xSn_{1-x}O_2$ ($x \leqslant 0.57$) exhibits *n*-type conductivities. For r-$Ge_xSn_{1-x}O_2$ ($x \leqslant 0.57$), as Ge compositions increase, the carrier concentrations and mobilities become higher and lower, respectively. In addition, even r-$Ge_xSn_{1-x}O_2$ with $x = 0.66$, 0.70, and 0.96 shows resistivities $<1\ \Omega$ cm.

We believe that our experimental and theoretical results give rise to fruitful information for further research and developments of the alloy system based on rutile-structured oxides as well as r-GeO_2, r-SnO_2, and r-SiO_2 for power-device applications.

The data that support the findings of this paper are available from the corresponding author upon reasonable request.

ACKNOWLEDGMENTS

This work was supported, in part, by JSPS KAKENHI Grant No. 21H01811. H.T. acknowledges JST, the Establishment of University Fellowships towards the Creation of Science Technology Innovation Grant No. JPMJFS2123.

[1] J. Y. Tsao, S. Chowdhury, M. A. Hollis, D. Jena, N. M. Johnson, K. A. Jones, R. J. Kaplar, S. Rajan, C. G. Van de Walle, E. Bellotti *et al.*, Adv. Electron. Mater. **4**, 160051 (2018).

[2] M. Orita, H. Ohta, and M. Hirano, Appl. Phys. Lett. **77**, 4166 (2000).

[3] T. Onuma, S. Saito, K. Sasaki, T. Masui, T. Yamaguchi, T. Honda, and M. Higashiwaki, Jpn. J. Appl. Phys. **54**, 112601 (2015).

[4] M. Stapelbroek and B. D. Evans, Solid State Commun. **25**, 959 (1978).

[5] S. Chae, J. Lee, K. A. Mengle, J. T. Heron, and E. Kioupakis, Appl. Phys. Lett. **114**, 102104 (2019).

[6] K. A. Mengle, S. Chae, and E. Kioupakis, J. Appl. Phys. **126**, 085703 (2019).

[7] C. A. Niedermeier, K. Ide, T. Katase, H. Hosono, and T. Kamiya, J. Phys. Chem. C **124**, 25721 (2020).

[8] K. Bushick, K. A. Mengle, S. Chae, and E. Kioupakis, Appl. Phys. Lett. **117**, 182104 (2020).

[9] S. Chae, K. A. Mengle, R. Lu, A. Olvera, N. Sanders, J. Lee, P. F. P. Poudeu, J. T. Heron, and E. Kioupakis, Appl. Phys. Lett. **117**, 102106 (2020).

[10] J. W. Goodrum, J. Cryst. Growth **7**, 254 (1970).

[11] D. E. Swets, J. Cryst. Growth **8**, 311 (1971).

[12] V. Agafonov, D. Michel, M. Perez y Jorba, and M. Fedoroff, Mater. Res. Bull. **19**, 233 (1984).

[13] S. Chae, H. Paik, N. M. Vu, E. Kioupakis, and J. T. Heron, Appl. Phys. Lett. **117**, 072105 (2020).

[14] H. Takane and K. Kaneko, Appl. Phys. Lett. **119**, 062104 (2021).

[15] G. Deng, K. Saito, T. Tanaka, M. Arita, and Q. Guo, Appl. Phys. Lett. **119**, 182101 (2021).

[16] A. Sasaki, M. Nishiuma, and Y. Takeda, Jpn. J. Appl. Phys. **19**, 1695 (1980).

[17] I. Akasaki and H. Amano, Jpn. J. Appl. Phys. **36**, 5393 (1997).

[18] O. Ambacher, J. Phys. D. Appl. Phys. **31**, 2653 (1998).

[19] K. Kaneko, T. Nomura, I. Kakeya, and S. Fujita, Appl. Phys. Express **2**, 075501 (2009).

[20] S. Fujita and K. Kaneko, J. Cryst. Growth **401**, 588 (2014).

[21] D. Fröhlich, R. Kenklies, and R. Helbig, Phys. Rev. Lett. **41**, 1750 (1978).

[22] T. Minami, Semicond. Sci. Technol. **20**, S35 (2005).

[23] W. Göpel and K. D. Schierbaum, Sensors Actuators B **26**, 1 (1995).

[24] T. Oshima, T. Okuno, and S. Fujita, Jpn. J. Appl. Phys. **48**, 120207 (2009).

[25] R. E. Presley, C. L. Munsee, C. H. Park, D. Hong, J. F. Wager, and D. A. Keszler, J. Phys. D. Appl. Phys. **37**, 2810 (2004).

[26] G. T. Dang, T. Uchida, T. Kawaharamura, M. Furuta, A. R. Hyndman, R. Martinez, S. Fujita, R. J. Reeves, and M. W. Allen, Appl. Phys. Express **9**, 041101 (2016).

[27] A. N. Trukhin, T. I. Dyuzheva, L. M. Lityagina, and N. A. Bendeliani, Solid State Commun. **131**, 1 (2004).

[28] J. Pascual, J. Camassel, and H. Mathieu, Phys. Rev. B **18**, 5606 (1978).

[29] W. H. Baur and A. A. Khan, Acta Crystallogr. Sect. B **27**, 2133 (1971).

[30] S. Fujita, Jpn. J. Appl. Phys. **54**, 030101 (2015).

[31] P. Giannozzi, S. Baroni, N. Bonini, M. Calandra, R. Car, C. Cavazzoni, D. Ceresoli, G. L. Chiarotti, M. Cococcioni, I. Dabo *et al.*, J. Phys. Condens. Matter **21**, 395502 (2009).

[32] P. Giannozzi, O. Andreussi, T. Brumme, O. Bunau, M. B. Nardelli, M. Calandra, R. Car, C. Cavazzoni, D. Ceresoli, M. Cococcioni *et al.*, J. Phys. Condens. Matter **29**, 465901 (2017).

[33] P. Blaha, K. Schwarz, F. Tran, R. Laskowski, G. K. H. Madsen, and L. D. Marks, J. Chem. Phys. **152**, 074101 (2020).

[34] A. R. Oganov and C. W. Glass, J. Chem. Phys. **124**, 244704 (2006).

[35] A. O. Lyakhov, A. R. Oganov, H. T. Stokes, and Q. Zhu, Comput. Phys. Commun. **184**, 1172 (2013).

[36] A. R. Oganov, A. O. Lyakhov, and M. Valle, Acc. Chem. Res. **44**, 227 (2011).

[37] J. P. Perdew, A. Ruzsinszky, G. I. Csonka, O. A. Vydrov, G. E. Scuseria, L. A. Constantin, X. Zhou, and K. Burke, Phys. Rev. Lett. **100**, 136406 (2008).

[38] G. Prandini, A. Marrazzo, I. E. Castelli, N. Mounet, and N. Marzari, npj Comput. Mater. **4**, 72 (2018).

[39] H. J. Monkhorst and J. D. Pack, Phys. Rev. B **13**, 5188 (1976).

[40] J. P. Perdew, K. Burke, and M. Ernzerhof, Phys. Rev. Lett. **77**, 3865 (1996).

[41] F. Tran and P. Blaha, Phys. Rev. Lett. **102**, 226401 (2009).

[42] D. Koller, F. Tran, and P. Blaha, Phys. Rev. B **85**, 155109 (2012).

[43] Y. Ota, AIP Adv. **10**, 125321 (2020).

[44] B. D. Pelatt, J. F. Wager, and D. A. Keszler, J. Solid State Chem. **274**, 337 (2019).

[45] M. Fukumoto, S. Nakao, K. Shigematsu, D. Ogawa, K. Morikawa, Y. Hirose, and T. Hasegawa, Sci. Rep. **10**, 6844 (2020).

[46] H. Takane and K. Kaneko, Appl. Phys. Lett. **120**, 099903 (2022).

[47] R. K. Ham, Philos. Mag. **6**, 1183 (1961).

[48] G. E. Jellison and F. A. Modine, Appl. Phys. Lett. **69**, 371 (1996).

[49] H. Chen and W. Z. Shen, Eur. Phys. J. B **43**, 503 (2005).

[50] M. Nagasawa and S. Shionoya, Phys. Rev. Lett. **21**, 1070 (1968).

[51] M. Nagasawa and S. Shionoya, J. Phys. Soc. Japan **30**, 1118 (1971).

[52] J. Tauc, R. Grigorovici, and A. Vancu, Phys. Status Solidi B **15**, 627 (1996).

[53] E. A. Davis and N. F. Mott, Philos. Mag. **22**, 903 (1970).

[54] A. D. Becke, J. Chem. Phys. **98**, 1372 (1993).

[55] J. P. Perdew, M. Ernzerhof, and K. Burke, J. Chem. Phys. **105**, 9982 (1996).

[56] J. Heyd, G. E. Scuseria, and M. Ernzerhof, J. Chem. Phys. **118**, 8207 (2003).

[57] L. Hedin, Phys. Rev. **139**, A796 (1965).

[58] F. Aryasetiawan and O. Gunnarsson, Rep. Prog. Phys. **61**, 237 (1998).

[59] Y. Kang, G. Kang, H. H. Nahm, S. H. Cho, Y. S. Park, and S. Han, Phys. Rev. B **89**, 165130 (2014).

[60] S. B. Zhang, S. H. Wei, and A. Zunger, J. Appl. Phys. **83**, 3192 (1998).

[61] S. B. Zhang, S. H. Wei, and A. Zunger, Phys. Rev. Lett. **84**, 1232 (2000).

[62] S. B. Zhang, J. Phys. Condens. Matter **14**, R881 (2002).

[63] A. Zunger, Appl. Phys. Lett. **83**, 57 (2003).

[64] J. Robertson and S. J. Clark, Phys. Rev. B **83**, 075205 (2011).

[65] W. Walukiewicz, Appl. Phys. Lett. **54**, 2094 (1989).

[66] W. Walukiewicz, J. Cryst. Growth **159**, 244 (1996).

[67] W. Walukiewicz, Phys. B **302–303**, 123 (2001).

[68] S. X. Li, K. M. Yu, J. Wu, R. E. Jones, W. Walukiewicz, J. W. Ager, W. Shan, E. E. Haller, H. Lu, and W. J. Schaff, Phys. Rev. B **71**, 161201(R) (2005).

[69] Ç. Kiliç and A. Zunger, Appl. Phys. Lett. **81**, 73 (2002).

[70] A. K. Singh, A. Janotti, M. Scheffler, and C. G. Van de Walle, Phys. Rev. Lett. **101**, 055502 (2008).

[71] P. D. C. King, R. L. Lichti, Y. G. Celebi, J. M. Gil, R. C. Vilão, H. V. Alberto, J. Piroto Duarte, D. J. Payne, R.

G. Egdell, I. McKenzie *et al.*, Phys. Rev. B **80**, 081201(R) (2009).
[72] H. Ehrenreich, J. Phys. Chem. Solids **12**, 97 (1959).
[73] L. Makowski and M. Glicksman, J. Phys. Chem. Solids **34**, 487 (1973).
[74] J. W. Harrison and J. R. Hauser, Phys. Rev. B **13**, 5347 (1976).
[75] B. Russo and G. Z. Cao, Appl. Phys. A **90**, 311 (2008).
[76] H. Iida, T. Mishuku, A. Ito, K. Kato, M. Yamanaka, and Y. Hayashi, Sol. Energy Mater. **17**, 407 (1988).